ORGANIC CHEMISTRY FRONTIERS

RESEARCH ARTICLE

View Article Online
View Journal

Cite this: DOI: 10.1039/d6qo00354k

Self-aggregation and host–guest behavior of tetraureido-substituted tetranitro-azacalix[4]arenes

Karolína Salvadori, *[a,b,c] Sabrina Pricl, [d,e] Aura Tintaru, [b] Alena Krupková, [c] Václav Eigner, [f] Pavel Matějka, [g] Pavel Lhoták [h] and Olivier Siri *[b]

The reaction of tetranitro-tetraminoazacalix[4]arene with a series of aromatic isocyanates leads to the formation of tetraureido-receptors, whose isolation was efficiently achieved (~80% yield) by organic solvent nanofiltration when conventional chromatographic methods proved ineffective. The receptors exhibit a pronounced tendency to self-aggregate in solution, and the extent and stability of the formed assemblies are strongly modulated by the nature of the aryl substituents. A combined experimental (dilution NMR, DOSY) and theoretical investigation revealed that dimer formation arises from a cooperative interplay between π–π interactions and hydrogen bonding, with aromatic stacking providing the dominant stabilizing contribution. Molecular dynamics simulations highlight significant differences in the stability of selected dimers, rationalizing their distinct aggregation tendencies. X-ray analysis reveals that while π–π stacking remains significant even in the solid state, the ureido motifs preferentially coordinate solvent molecules. Importantly, receptor self-association does not prevent anion recognition. Even in the strongly hydrogen-bond-competitive solvent (DMSO), the receptors efficiently bind anions, exhibiting a selectivity sequence $H_2PO_4^-$ > BzO^- > AcO^- ≫ Cl^-, that cannot be rationalized solely by anion basicity. These findings demonstrate that tetraureido tetranitro-azacalix[4]arene architectures represent substitution-tunable supramolecular systems that combine controlled self-assembly with robust anion complexation ability.

Received 19th March 2026,
Accepted 28th April 2026

DOI: 10.1039/d6qo00354k

rsc.li/frontiers-organic

Introduction

Negatively charged species play fundamental roles in numerous biological and environmental processes. In particular, basic anions such as phosphates[1,2] and carboxylates[3,4] are key components of numerous biochemical pathways, and disruption of their balance can lead to significant physiological and ecological effects. Consequently, the design, synthesis, and investigation of artificial anion receptors have become an important area of research in supramolecular chemistry,[5] with the primary aim of achieving efficient and selective anion recognition in solution.[6]

Among the various anion-binding motifs explored to date, ureido groups have attracted considerable attention as versatile supramolecular units, combining strong and highly directional hydrogen bonding with a relatively low propensity for deprotonation.[7] Compared with amide-based receptors,[8] which often display weaker binding, and with more acidic donors such as thioureas[9] and sulfonamides[10] that may undergo deprotonation in the presence of basic anions, ureido-based systems provide an optimal balance between binding strength and chemical stability.

Early approaches to receptor design predominantly focused on podand-type systems, including open-chain monoureido structures (Fig. 1, compound **A**). Despite their structural simplicity, several derivatives were shown to form well-defined intermolecular assemblies governed by complementary N–H···O hydrogen bonds and π–π interactions between aromatic units.[11,12] In terms of anion-binding properties, various bis

[a]Department of Analytical Chemistry, University of Chemistry and Technology, Prague (UCTP), Technicka 5, 166 28 Prague 6, Czech Republic. E-mail: salvadok@vscht.cz
[b]Aix-Marseille Université, CNRS UMR 7325 Centre Interdisciplinaire de Nanoscience de Marseille (CINaM), Campus de Luminy, Marseille cedex 09 13288, France. E-mail: olivier.siri@univ-amu.fr
[c]Institute of Chemical Process Fundamentals of Czech Academy of Sciences v.v.i., Rozvojová 135, Prague 6, 16502, Czech Republic
[d]Molecular Biology and Nanotechnology Laboratory (MolBNL), Department of Engineering and Architecture (DIA), University of Trieste, Piazzale Europa 1, 34127 Trieste, Italy
[e]Department of General Biophysics, Faculty of Biology and Environmental Protection, University of Lodz, ul. Pomorska 141/143, 90-236 Łódź, Poland
[f]Institute of Physics AS CR, v.v.i., Na Slovance 2, 182 21 Prague 8, Czech Republic
[g]Department of Physical Chemistry, University of Chemistry and Technology, Prague (UCTP), Technicka 5, 166 28 Prague 6, Czech Republic
[h]Department of Organic Chemistry, University of Chemistry and Technology, Prague (UCTP), Technicka 5, 166 28 Prague 6, Czech Republic

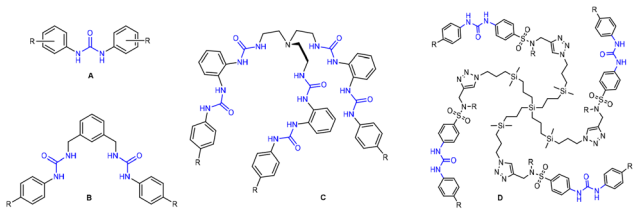

Fig. 1 Selected examples of (poly)-ureido derivatives.

(phenyl)urea receptors have been extensively studied. For example, it has been shown that bis(4-nitrophenyl)ureido receptor **A** binds anions in acetonitrile primarily according to their basicity (K_{As}): $AcO^- > BzO^- > H_2PO_4^- > NO_2^- > HSO_4^- > NO_3^-$.[13]

The incorporation of additional functional elements to modulate solubility, aggregation propensity, binding affinity, and selectivity represents a natural step in the evolution of ureido-based receptors. On this basis, more complex polyureido architectures have been developed, in which multiple ureido motifs are preorganized through linkers such as *m*-phenylene units[14] or anchored to flexible scaffolds, including tris(2-aminoethyl) amine[15–17] and dendrimer-based frameworks[18,19] (Fig. 1, **B**–**D**).

A further conceptual step involves macrocyclic platforms,[20] where preorganization improves recognition efficiency by minimizing the entropic penalty of binding, and an appropriate degree of structural rigidity ensures high binding affinity while simultaneously suppressing non-specific interactions.

Within macrocyclic receptors, the ureido motif can fulfil different structural roles: they may constitute integral components of macrocyclic frameworks (like glycoluril in bambusuril[21]), serve as a bridging element embedded within the macrocyclic backbones (*e.g.* **E**,[22] **F**[23]), or function as an appended binding site on preorganized scaffolds (*e.g.* **G**,[24] **H**[25]). These distinct design strategies enable precise control over the cavity size, shape, or spatial orientation of the binding sites, rendering ureido-containing macrocycles particularly attractive for advanced host–guest chemistry. However, while multivalent ureido architectures offer enhanced recognition capability, they are inherently susceptible to pronounced self-aggregation.[26] This often-overlooked phenomenon can complicate both purification and the reliable interpretation of binding data. Despite these challenges, the practical and conceptual importance of developing new, effective ureido-based anion receptors remains undeniable (Fig. 2).

Our recent work[27] described a series of acyclic and macrocyclic anion receptors containing 4-*tert*-butylphenylureido

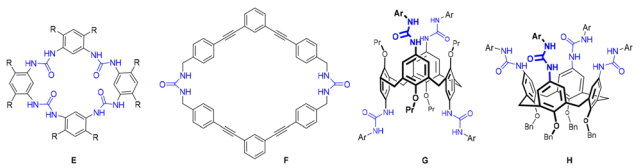

Fig. 2 Examples of macrocyclic receptors featuring ureido motif as a bridging element (**E**, **F**), or appended unit (**G**, **H**).

motifs and demonstrated that modulation of the electron-density distribution of the supporting scaffold strongly influences interactions with basic anions, leading either to undesired deprotonation (in acyclic systems) or to anion complexation (in macrocyclic receptors). Building on these findings, the present study reports a new family of tetraureido derivatives preorganized on a tetranitro-azacalix[4]arene platform, with particular emphasis on elucidating the relationship between the nature of the aryl substituent and the resulting supramolecular properties, including both host–host aggregation and host–guest anion recognition.

Results and discussion

The design of receptors presented herein is based on the premise that tetranitro-azacalix[4]arene adopts *1,3-alternate* conformation (using common calixarene nomenclature),[28] maintained even in solution. This conformation provides favorable spatial arrangement of binding sites for the preparation of potent anion hosts. The synthetic procedure for 4-*tert*-butylphenylureido receptor **6B** was described in our previous work,[27] and its extension to related derivatives is outlined in Scheme 1. Briefly, the preparation of tetranitro-azacalix[4]arene platform begins with nucleophilic aromatic substitution of fluorine in DFDNB (1,5-difluoro-2,4-dinitrobenzene) **1** with freshly prepared tetraaminobenzene tetrahydrochloride **3** in the presence of base. The tetranitro-tetraamino azacalix[4]arene **5** was obtained in good yields either *via* a stepwise route through intermediate **4** or by a direct one-pot procedure. Introduction of the urea moieties was achieved by reacting the amino groups with the appropriate aromatic isocyanate (2 molar equivalents per free $-NH_2$ group).

The crude reaction mixtures containing isocyanate decomposition by-products (mainly symmetric ureas **7**) were initially purified by preparative thin-layer chromatography (prep-TLC) on silica gel, affording isolated yields of approximately 70% for several derivatives. However, for some tetraureido derivatives (**6C** and **6E**), chromatographic purification proved inefficient. This difficulty can be attributed to the limited solubility of these compounds in common solvents. To overcome these limitations, organic solvent nanofiltration (OSN) using a regenerated cellulose membrane[29] was employed. This alternative purification strategy exploits the molecular size difference between the target receptors and impurities. For **6C** (Fig. S13), dissolution of the crude reaction mixture in DMF diluted with MeOH to decrease viscosity (and to disrupt hydrogen bonding between product and impurities) allowed filtration through the membrane. The progress of the separation was followed by checking the color of the filtrate. Here, 5–6 filtration cycles were sufficient to obtain pure **6C**, recovered from the retentate in approximately 80% yield.

Following the purification, the structures of receptors **6A–E** were confirmed by a combination of nuclear magnetic resonance (NMR) spectroscopy and high-resolution mass spectrometry (HRMS) techniques. The choice of solvent played a

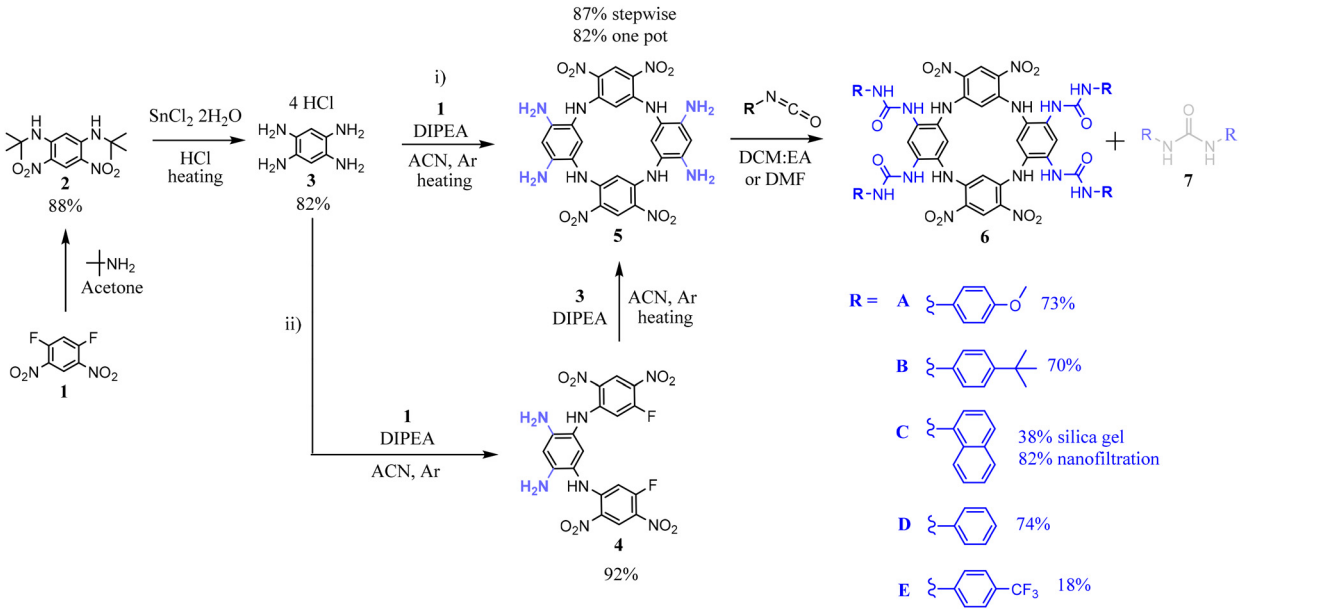

Scheme 1 Synthesis of tetra-ureido tetranitro-azacalix[4]arene derivatives **6**. The tetranitro-tetraamino azacalix[4]arene **5** was prepared *via* a one-pot reaction (i); or a stepwise approach (ii), with an overall yield of *ca*. 80%. The tetraaminobenzene tetrahydrochloride **3**, is commercially available or can be prepared as depicted, enabling straightforward access to the azacalix[4]arene platform.

key role in the NMR analysis (Fig. S23), and highly competitive DMSO-d_6 was employed to gain well-resolved spectra. In the ^{1}H NMR records, all receptors **6** displayed characteristic signals corresponding to the macrocyclic platform, including the bridging NH protons (~9.5 ppm) and 4 singlets assigned to the aromatic C–H protons of azacalix[4]arene (~9.1; 8.7; 7.1 and 5.5 ppm). In addition, two singlets corresponding to the ureido NH protons and the anticipated aromatic signals of the substituents were observed. The spectral patterns are consistent with the expected C_2 symmetry of the products.

Despite this overall similarity, noticeable differences were observed among derivatives **6A–E**. Particularly, in concentrated solutions, the aromatic signals appeared broadened and poorly resolved (Fig. 3a and Fig. S24), suggesting a dynamic process in solution. Upon heating to higher temperatures (Fig. S13b), these features gradually changed, with the aromatic C–H bond signals sharpening, while the ureido NH signals showed noticeable shifts. These observations pointed to a temperature-dependent equilibrium, likely associated with intermolecular interactions. To further investigate this behavior, concentration-dependent ^{1}H NMR experiments were conducted to evaluate the potential self-aggregation of these compounds. With the exception of receptor **6A**, bearing a strong electron-donating substituent, dilution-induced upfield shifts of the ureido NH signals, consistent with partial dissociation of self-aggregated species (Fig. S26–S29), were observed. Analysis of the dilution data using Bindfit software[30] afforded corresponding equilibrium constants K following the order **6C** ≫ **6E** > **6D** > **6B** (Table S1), clearly indicating substituent-dependent aggregation strength.

Based on these results, receptor **6C** was selected for further investigation of its aggregation behavior. Due to the strong absorption and fluorescence arising from the naphthyl moieties, dynamic light scattering (DLS) measurements were not feasible. Instead, concentration-dependent diffusion-ordered spectroscopy (DOSY) NMR experiments[31] were carried out. As shown in Fig. 3b, increasing the concentration of **6C** leads to slower diffusion, whereas the solvent diffusion remains unchanged. The appearance of new signals at more negative log D values at higher concentration indicates the formation of larger species. Then, the values of the hydrodynamic radii R_h for the molecular species in solution were estimated using the Stokes–Einstein equation (eqn (1)):

$$R_h = \frac{k_B T}{6\pi\eta D} \quad (1)$$

where R_h is the hydrodynamic radius of the molecular species, k_B is the Boltzmann constant, T is the absolute temperature, η is the solvent viscosity, and D is the diffusion coefficient. Approximate values of R_h = 0.35 nm (log D = −9.5) in diluted solution and R_h ≈ 0.9–1.1 nm (log D = −9.9 to −10) at higher concentration are consistent with the formation of small self-associate aggregates.

To gain molecular-level insight into the distinct aggregation behavior of **6C** and the less-aggregating receptor **6B**, molecular dynamics (MD) simulations were performed on their dimeric assemblies in explicit DMSO (Fig. S30), where solvent effects and molecular flexibility play a dominant role. The structural stability of the dimers was evaluated by monitoring several descriptors along the trajectories, including the total number of intradimer hydrogen-bond (HB)contacts, the fraction of native contacts (Q), the center-of-mass distance between monomers ($d_{COM-COM}$), and π–π stacking parameters (Fig. 4).

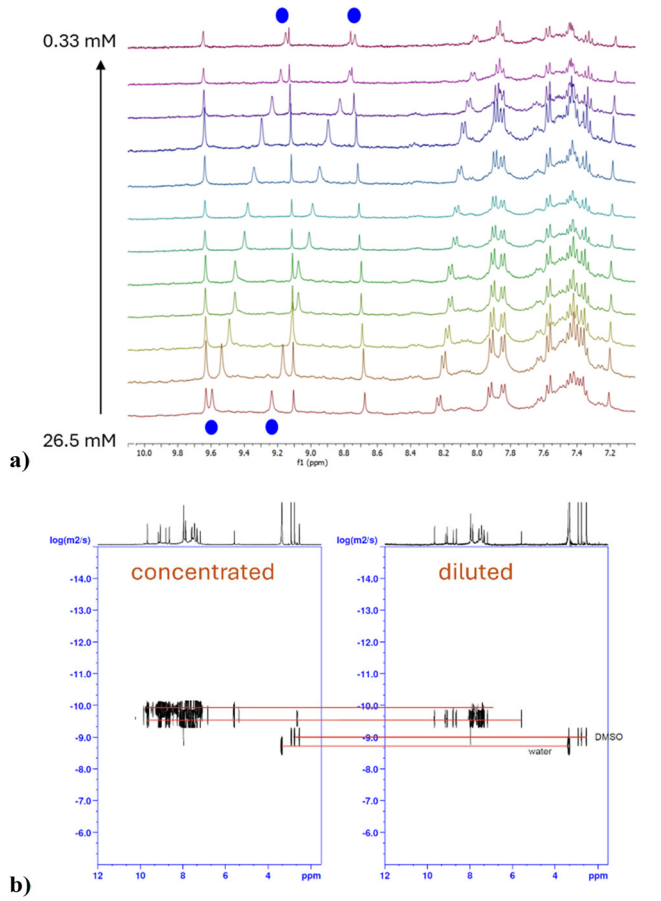

Fig. 3 (a) Part of ^{1}H NMR spectra (400 MHz, DMSO-d_6) of compound **6C** corresponding to the region containing ureido NH hydrogens (indicated by blue spots) and aromatic signals during dilution study. (b) DOSY records for compound **6C** at two different concentrations (concentrated = 11.0 mM; diluted = 1.6 mM) in DMSO-d_6.

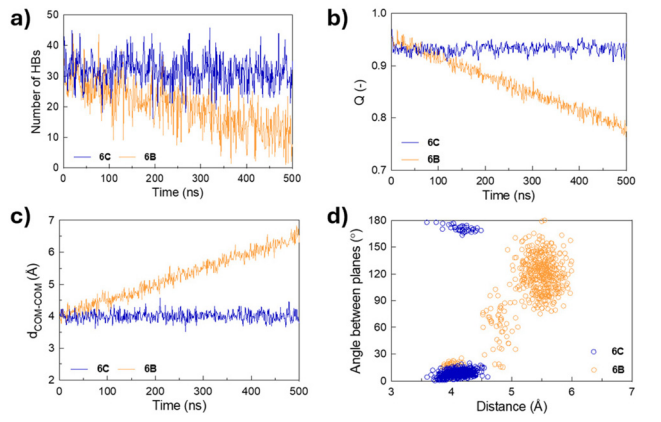

Fig. 4 (a) Total number of intradimer hydrogen bonds (HB) contact in the **6C** and **6B** dimers as a function of MD simulation time. (b) Native contact fraction (Q) for the **6C** and **6B** dimers as a function of time, as extracted from the relevant MD trajectories. (c) Time evolution of the center-of-mass distance ($d_{COM-COM}$) between the two macrocyclic units in the **6C** and **6B** dimers during the corresponding MD simulations. (d) Interplanar distances and angles between the aromatic units of the macrocyclic dimers **6C** and **6B** as extracted from the MD trajectories.

The evolution of intradimer HB contacts provides an initial measure of interfacial cohesion (Fig. 4a). The **6C** dimer maintains a consistently high number of HB contacts throughout the 500 ns simulation, with only limited fluctuations. These persistent HBs likely contribute to the overall structural integrity of the assembly, helping to orient the aromatic platforms in a favorable geometry for aggregation. In contrast, **6B** shows a gradual decline in intradimer HBs over time, indicative of reduced internal stabilization.

Analysis of the native contacts fraction (Q) further highlights the divergent stability profile of the two systems (Fig. 4b). For **6C**, Q remains high and nearly constant (~0.93), indicating preservation of the initial inter-residue contacts defining the dimer interface. This stability suggests minimal conformational drift and supports a compact, native-like organization across the entire trajectory. Conversely, **6B** exhibits a continuous and marked decline in Q (from ~0.95 to ~0.75), reflecting progressive disruption of the interface and structural rearrangement. The observed behavior is likely caused by internal strain and steric hindrance from the bulky *tert*-butyl groups, which impede maintenance of a stable dimer.

The evolution of the center-of-mass distance ($d_{COM-COM}$) between monomers provides a direct measure of supramolecular association (Fig. 4c). In the case of **6C**, $d_{COM-COM}$ remains remarkably stable at approximately 4.0 Å, indicating that the two macrocycles remain tightly associated. In contrast, **6B** displays a pronounced and progressive increase in $d_{COM-COM}$, ultimately exceeding 6.0 Å. This behavior is consistent with partial separation of the monomers and gradual loss of compact dimer organization.

The analysis of π–π stacking geometries provide insight into the aromatic interactions stabilizing the dimers (Fig. 4d). The **6C** dimer exhibits a narrow and well-defined distribution of interplanar distances (3.5–4.5 Å) and angles (<30° or >150°), consistent with a persistent face-to-face stacking arrangement. This ideal geometry is maintained throughout the simulation and is likely a key contributor to the overall rigidity and cohesion of the **6C** assembly. On the other hand, **6B** displays a broader and more scattered distribution of stacking parameters. Although the initial geometry briefly falls within the optimal range, the stacking progressively deteriorates over time, with interplanar distances increasing and angles becoming highly variable. This pattern reflects a gradual loss of π–π overlap, most likely due to steric hindrance imposed by the *tert*-butyl substituents, which interfere with close aromatic alignment. The resulting differences appear to be rooted in both electronic and steric effects: while the planar, extended aromatic surface of **6C** facilitates effective stacking and compact assembly, the bulkier architecture of **6B** disrupts optimal packing, leading to dynamic instability and impaired supramolecular integrity.

To complement the structural insights, component-wise decomposition of the binding free energies was performed using the Molecular Mechanics/Poisson-Boltzmann Surface Area (MM/PBSA) approach (Fig. 5a).[32] In both systems, the van

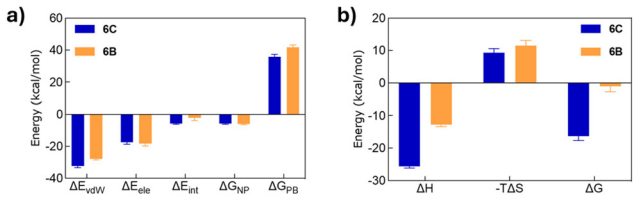

Fig. 5 (a) Decomposition of the binding enthalpy (ΔH), as obtained within the MM/PBSA framework, into its individual components for dimers **6C** and **6B**. The entalpic term is computed as the sum of van der Waals (ΔE_{vdW}), electrostatic (ΔE_{ele}), internal (ΔE_{int}), polar solvation (ΔG_{PB}), and nonpolar solvation (ΔG_{NP}) contributions. (b) Comparison of the overall binding enthalpy (ΔH), entropy ($T\Delta S$) and the resulting binding free energy ($\Delta G = \Delta H - T\Delta S$) for **6C** and **6B**.

der Waals term (ΔE_{vdW}) dominates the stabilizing contributions. Notably, **6C** exhibits a significantly stronger ΔE_{vdW}, consistent with tight aromatic stacking. The electrostatic interaction energy (ΔE_{ele}) is slightly more favorable in **6B**; but insufficient to compensate for the weaker ΔE_{vdW} contribution. As a result, the overall non-covalent interaction profile remains clearly more favorable for **6C**. The internal energy term (ΔE_{int}), which includes bond, angle, and dihedral contributions, is also slightly more stabilizing in **6C**. This suggests that **6C** maintains a more favorable internal geometry upon dimerization, with less conformational strain compared to **6B**. The lower ΔE_{int} contribution observed in **6B** may ultimately reflect suboptimal alignment of the monomeric units and internal distortion required to maintain contact. As expected, the polar solvation free energy (ΔG_{PB}) introduces a positive penalty in both dimers, as polar groups become partially buried. Nevertheless, this cost is better compensated in **6C** due to stronger non-covalent stabilization. The nonpolar solvation energy (ΔG_{NP}) is minor in magnitude but still more favorable in **6C**, consistent with a greater solvent-excluded surface upon dimerization.

Fig. 5b compares the overall binding enthalpy (ΔH) and free energy (ΔG) for the **6C** and **6B** dimers. While both dimers experience an entropic penalty associated with reduced configurational freedom, **6C** retains a substantially more favorable free energy of binding ($\Delta G = -16.3 \pm 1.3$ kcal mol^{-1}), confirming its superior thermodynamic stability. For **6B**, the weaker enthalpic stabilization is compounded by the entropic penalty, resulting in a significantly less favorable ΔG (-1.1 ± 1.6 kcal mol^{-1}). Although MM/PBSA estimates should be interpreted in a comparative rather than absolute sense, the energetic trends are consistent with both the structural descriptors and experimental data, and support the conclusion that **6C** forms a persistent, compact dimer in solution, whereas **6B** lacks the capacity to sustain stable supramolecular association under comparable conditions.

Taken together, the MD simulations provide a coherent picture of the marked difference in supramolecular stability between the two systems. Receptor **6C** forms a persistent π–π stacked dimer stabilized by intradimer hydrogen bonding and a compact, complementary interface. By contrast, **6B**, although initially dimeric, undergoes progressive disassembly over time. These divergent behaviors stem from a combination of electronic and steric factors: the planar, extended aromatic core of **6C** favors efficient stacking and tight molecular packing, whereas the bulkier substituents in **6B** hinder optimal interfacial alignment, ultimately compromising dimer stability. These computational findings are consistent with experimental results from dilution NMR and binding assays, offering a molecular-level rationale for the differential behavior observed for these two macrocyclic receptors in DMSO solution.

Alongside the investigation of host–host interactions of **6C** in solution, we aimed to examine its solid-state structure by X-ray diffraction analysis. Although intermolecular packing in the crystal does not necessarily mirror behavior in solution, owing to the fundamentally different physical environments of the two phases, the solid-state analysis provides complementary structural insight and may help contextualize the observed intermolecular interactions. Initial crystallization attempts from DMSO and various other solvents and their mixtures, including acetone, acetonitrile, and ethyl acetate, did not yield crystals of sufficient quality. Slow evaporation from a DMF/hexane mixture ultimately proved successful, affording single crystals suitable for diffraction studies.

The macrocycle **6C** crystallized in a monoclinic crystal system, space group $P2_1/n$, forming a 1 : 5 solvate with DMF molecules. As shown in Fig. 6a and b, the azacalix[4]arene skeleton adopts the expected *1,3-alternate* conformation in the solid state. Two nitro-substituted aromatic moieties are extremely flattened with the corresponding interplanar angles (Φ) of 155.30° and 145.95° (towards the main plane of the molecule defined by the four nitrogen bridging atoms). The remaining urea-bearing subunits are nearly perpendicular to the main plane (Φ = 80.82° and 81.88°), resulting in their slight tilt towards the cavity. The structure is fixed by a quadruple intramolecular hydrogen bond between the oxygen of the nitro group and the proximal N–H bond of the bridging nitrogen with corresponding N–H···O distances ranging from 1.910 to 2.062 Å (Fig. 6b).

The crystal packing of **6C** is characterized by a large number of non-covalent interactions, which cannot be listed in a simple way. However, some general conclusions can be drawn. First of all, urea groups are practically excluded from intermolecular HB interactions, since each of these groups is involved in complexation of solvent molecules through the interaction of both NH bonds with the DMF carbonyl oxygen (Fig. 6c). Depending on the specific bonded partners, the NH···O=C distances range from 1.935 to 2.454 Å. The molecules of **6C** are linked to each other by several different types of aromatic interactions.[33,34] Fig. 6d shows the dimeric motif based on π–π interactions between the naphthyl and tetraamine fragments. Both aromatic systems adopt a practically coplanar arrangement with at least six C···C close contacts (from 3.360 to 3.527 Å), corresponding to the typical interplanar distances in aromatic interactions (3.5 Å). The importance of naphthyl groups in the packing of **6C** can be demonstrated

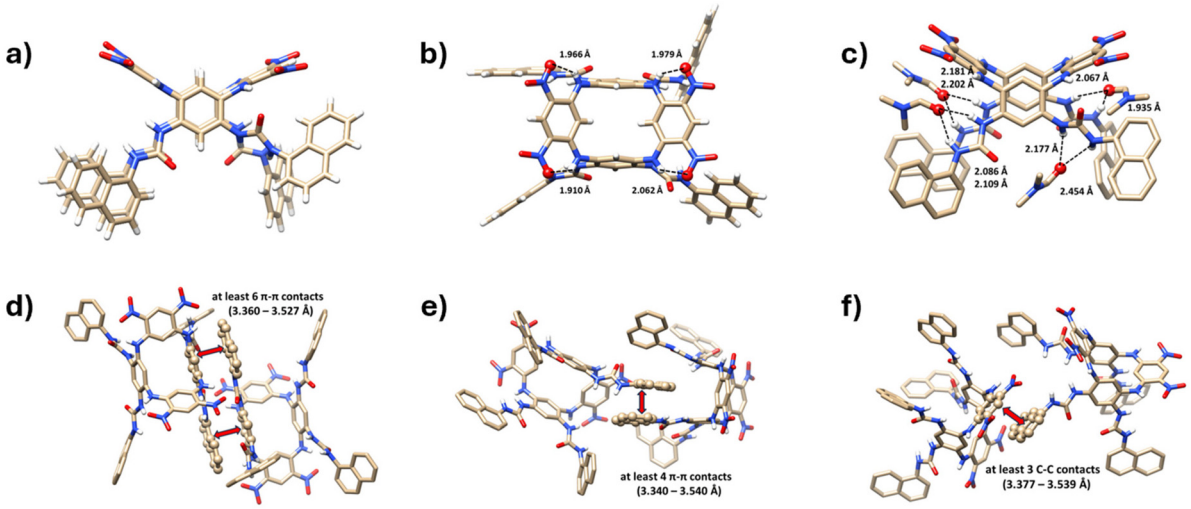

Fig. 6 Single crystal X-ray structure of compound **6C**: (a) side-view; (b) top-view showing intramolecular HBs between the NH and NO_2 groups; (c) complexation of DMF molecules *via* HBs with urea functions (the interacting atoms shown as balls); (d) π–π interactions between naphthalene and tetramino fragments; (e) π–π interactions between the naphthalene moieties; (f) π–π interactions between naphthalene and dinitroaromatic subunit (the interacting coplanar aromatic systems shown as balls).

on the π–π interactions between these aromatic units. Fig. 6e shows a dimeric motif based on at least four close contacts (3.340 to 3.540 Å) between carbon atoms of the naphthalene moieties. In addition, another type of π–π interactions can be observed between the coplanar naphthyl and dinitro fragments of the macrocycle (Fig. 6f).

Following the analysis of host-host interaction, the anion-binding properties of receptors **6** were investigated. UV–Vis spectroscopy was used to distinguish between hydrogen-bond-assisted complexation and receptor deprotonation. Only moderate spectral changes were observed upon addition of basic anions (Fig. S31a–S37a), whereas DBU (1,8-diazabicycloundec-7-ene) induced pronounced absorbance changes (Fig. S31b–S33b and S36b–S37b). This contrast indicates that anion recognition proceeds *via* complexation rather than receptor deprotonation.

UV–Vis spectroscopy was suitable to distinguish receptor deprotonation from anion binding, but showed only a weak response to anions, limiting further insight into binding interactions. Therefore, ^{1}H NMR spectroscopy was employed to probe anion binding preferences (Fig. 7a). As expected, large and diffuse anions such as I^-, ClO_4^- and PF_6^- exhibited negligible interaction with ureido binding sites, as evidenced by the absence of chemical-shift changes in the ureido NH signals. This lack of interaction can be attributed to their low charge density and poor hydrogen-bond-accepting ability.

Slightly stronger, yet still moderate, interactions were observed for stabilised non-basic anions (Cl^-, HSO_4^- and NO_3^-). Saturation in titration experiments required either a high anion excess or elevated concentrations. Regarding the complex stoichiometry, continuous variation analysis[35,36] was used. For chloride, Job plot (Fig. S48–S52) showed maxima near 0.2 for all receptors, consistent with multiple independent binding events and an apparent 1 : 4 receptor–anion ratio. This is supported by the unchanged diagnostic signals of the macrocyclic platform (C–H between nitro groups) throughout the titrations (Fig. 7c and Fig. S38–S42), indicating that chloride binding does not induce significant changes in scaffold geometry. Overall, non-basic anions exhibiting weak interactions without significant advantages coming from the macrocyclic skeleton.

In contrast, basic anions induced pronounced spectral changes (Fig. 7a, c and Fig. S43–S47), indicating complexation-driven response of the receptor. Significant shifts were observed in both the ureido NH and macrocyclic C–H signals, consistent with conformational adaptation of the azacalixarene scaffold. Signal broadening in some cases prevented precise assignment, but the overall spectral characteristics indicate a cooperative and geometrically demanding binding process compared to non-basic anions. Job plot analysis revealed maxima between 0.33 and 0.5 depending on the receptor substituent and the anion (Fig. S48–S52), suggesting deviations from simple independent-site binding. For **6A** and **6B**, which exhibit minimal aggregation and reduced hydrogen-bond donating ability, consistent maxima at ~0.33 were observed for all basic anions, corresponding to a 1 : 2 (receptor-to-anion) stoichiometry. In contrast, **6C–6E** displayed shifted or broadened maxima, likely reflecting multiple coexisting equilibria and higher-order binding modes.

Given this complexity, the raw NMR data were primarily presented graphically (Fig. 7b and Fig. S53), analysing the percentage of *CIS* values and the shapes of the binding isotherms for qualitative comparison. To compare selectivity, receptors **6B** and **6C** were examined under identical conditions (1.2 mM receptor concentration, comparable anion equivalents). Fig. 7b (Fig. S53) reveals the selectivity sequence $H_2PO_4^-$ > BzO^- >

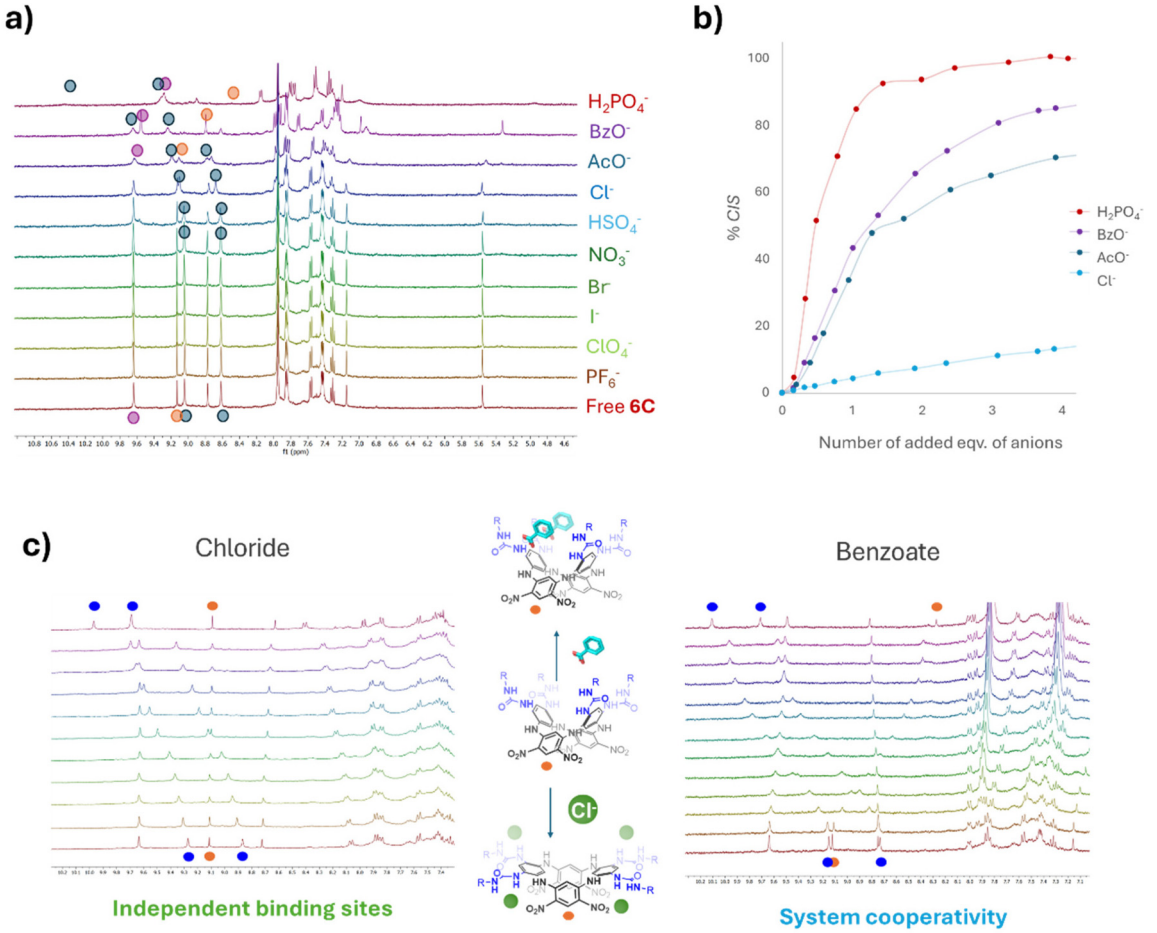

Fig. 7 (a) Part of aromatic and NH region in ^{1}H NMR records of receptor **6C** (1.19 mM) with 1 eq. of an appropriate anion with highlighted urea NH hydrogens (blue), NH bridge (pink), and diagnostic aromatic C–H signal corresponding to the macrocycle (orange). (b) Binding efficiency (% *CIS* analysis) of selected anions with receptor **6C** (details corresponding to all concentrations used and remaining titration points are summarised in SI – page S41–S44). (c) Schematic representation of complexation together with ^{1}H NMR titrations of receptor **6C** (DMSO-d_6, 400 MHz, 298 K) with TBACl or TBABzO. Highlighted signals correspond to urea NH hydrogens (blue) and diagnostic aromatic signals corresponding to the macrocycle (orange; spatially distant from the binding site, making direct electronic effects less likely). For more details regarding concentrations, see pages S29 and S41 of the SI.

$AcO^- \gg Cl^-$, indicating that factors beyond simple basicity contribute to anion coordination. A possible rationale for the observed affinity increase lies in the propensity of $H_2PO_4^-$ to dimerize within a well-preorganized supramolecular complex/assembly.[37] Notably, the differences among individual anions were more pronounced for **6C**.

To examine substituent effects, benzoate was chosen as a representative guest. Although it is strongly bound, benzoate is not the most tightly coordinated anion, thereby allowing the influence of individual substituents to be clearly distinguished (Fig. 8). Receptor **6E**, ($-CF_3$ substituent) exhibited the highest binding efficiency, consistent with the positive influence of electron-withdrawing groups on hydrogen-bond donation and, hence, binding strength. Receptors **6C** and **6D** reached approximately 85% of the *CIS* value upon addition of four equivalents of benzoate. However, it should be noted that their titration profiles differ, as receptor **6C** forms significantly

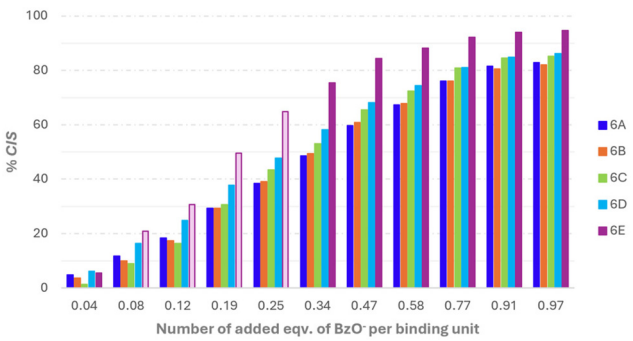

Fig. 8 Binding efficiency of receptors **6** (1.2 mM) expressed as a percentage of the maximal value of *CIS*, depending on the equivalent of TBABzO (anion to binding unit ratio). The data for **6E** in the interval between 0.08–0.25 eq. per binding site are displayed with a light color because of the NH broadening – inaccuracy in the determination of signal position.

Table 1 Values of (apparent) association constants K_{As} (1 : 1) and (apparent) overall association constants β, which were determined by ^{1}H NMR in DMSO-d_6 with a series of receptors **6** and TBABzO

Receptor	K_{As} (1 : 1)[a]	β[b]
6A[c]	2530	1.60×10^6
6B	2520	1.59×10^6
6C	4000	4.00×10^6
6D	6490	1.05×10^7
6E	8400	1.76×10^7

[a] Error, when estimated, was <30%. [b] β values were calculated for 1 : 2 stoichiometry using a statistical model, where: $\beta = K_{As}$ (1 : 1) × K_{As} (1 : 2), and K_{As} (1 : 2) = K_{As} (1 : 1)/4. [c] Represents the case in which no detectable self-aggregation occurs, and therefore its behavior can be described as a host–guest association process.

stronger and more stable self-aggregates. The weakest binding was observed for receptors bearing electron-donating groups (*tert*-butyl or –OMe), in agreement with expectations based on their reduced hydrogen-bond donating ability.

Finally, despite the varying Job plot outcomes, quantitative analysis of titration data was attempted using classical 1 : 2 host–guest binding models[38] (Table 1). While this approach adequately described the data for receptors **6A** and **6B**, lower quality fits were obtained for the remaining receptors. For the receptors **6B–6E**, self-aggregation is present, and the observed behavior reflects a competition/interplay between host–host and host–guest interactions. The results indicate that the binding constants derived for **6B–6E** should be regarded as effective parameters rather than precise thermodynamic descriptors. Nevertheless, the trends correlate with ureido hydrogen-bond donating ability and provide a meaningful comparison of relative binding efficiencies across the receptor series.

Conclusions

In conclusion, a series of tetraureido azacalix[4]arene receptors in which the nature of the aromatic substituent governs both self-assembly and anion-recognition properties was presented. The purification was achieved not only by conventional chromatography but also through nanofiltration, providing a practical strategy for handling highly aggregating and poorly soluble supramolecular host systems. Combined experimental and computational analyses demonstrate that these receptors undergo substituent-dependent self-aggregation in solution, even in strongly competitive DMSO. Molecular dynamics simulations reveal that π–π stacking interactions, supported by cooperative hydrogen bonding, play a dominant role in stabilizing persistent dimeric assemblies, particularly for derivative **6C**. Importantly, self-aggregation does not preclude anion recognition. The receptors effectively bind basic anions, with binding efficiency modulated by the electronic nature of the substituents and increasing with hydrogen-bond-donating ability. The observed selectivity sequence, which cannot be rationalized solely by anion basicity, further underscores the role of structural preorganization and supramolecular cooperativity. In summary, this study demonstrates that controlled substitution on a preorganized tetranitro-azacalix[4]arene scaffold enables fine-tuning of both host–host and host–guest equilibria, providing a versatile platform for the design of responsive supramolecular receptors.

Experimental

General experimental procedures

All commercially available reagents were purchased from standard suppliers and were used without further purification unless otherwise stated. Solvents were dried and stored according to standard procedures for anhydrous conditions. Analytical thin-layer chromatography (TLC), used to monitor the progress of reactions, was performed on silica gel 60 F_{254} aluminum sheets (Merck). Visualization was carried out under UV light at 254 nm. Preparative thin-layer chromatography (prep-TLC) was performed on self-prepared glass plates (20 × 20 cm) coated with silica gel 60 PF_{254} (Merck). This method was employed for the isolation of urea derivatives **6** from crude reaction mixtures containing residual impurities, primarily arising from the decomposition of the corresponding aromatic isocyanates.

Organic solvent nanofiltration. OSN was carried out in a semicontinuous dead-end setup, using solvent-resistant stirred cell equipped with 1 kDa molecular weight cut-off regenerated cellulose ultrafiltration disc Ultracel® (both Millipore, Merck KGaA, Darmstadt, Germany) and PTFE coated O-rings (ERIKS), with nitrogen as a driving gas at transmembrane pressure 4.5–5.0 bar. The separated mixture dissolved in DMF was quantitatively transferred into the cell and diluted with MeOH to achieve 1 : 2 DMF : MeOH (v : v) solvent ratio. The initial volume of 10–15 mL was reduced to approx. 1/10 and the retentate was diluted by fresh solvent mixture. This cycle was repeated until there was no detectable impurity in the filtrate (5–6 times).

All prepared compounds were characterized by multinuclear NMR (^{1}H NMR, ^{13}C NMR, and ^{19}F NMR), IR spectroscopy, and high-resolution mass spectrometry (HRMS). Detailed spectroscopic data and copies of the spectra are provided in the SI.

Spectral characterisations

NMR spectroscopy. The ^{1}H (400.1 MHz), ^{13}C (100.6 MHz), and ^{19}F (376.5 MHz) spectra were recorded using a Bruker Avance 400 spectrometer or JEOL ECS 400 MHz spectrometer at 25 °C. The ^{1}H and ^{13}C NMR spectra were referenced to the residual solvent signal (δ/ppm; δ_H/δ_C: DMSO-d_6, 2.50/39.52 ppm; δ_H: $CDCl_3$ 7.26 ppm; solvents stored over molecular sieves). In some spectra, a signal corresponding to tetramethylsilane (TMS), present in the solvent, is observed. The ^{19}F spectra were referenced to the line of external standard hexafluorobenzene (δ_F/ppm; −163.00). Chemical shifts (δ) are reported in parts per million (ppm) and coupling constants (J) are given in Hertz (Hz). Data are reported as follows: chemical

shift, multiplicity (s – singlet, d – doublet, t – triplet, dd – doublet of doublet, m – multiplet, brs – broad signal), integration, and coupling constant. Spectra were processed using MestReNova 15.0.1. software.

IR spectroscopy. FTIR spectra were recorded on a Nicolet iS50 spectrometer (Thermo-Nicolet, USA) connected with a GladiATR diamond placed outside the conventional sample compartment, equipped with DTGS KBr detector. Reflectance data were acquired with the following parameters – spectral range: 4000–400 cm^{-1}, resolution: 4 cm^{-1}, number of spectra accumulations: 64, apodization: Happ-Genzel. The spectra were collected and processed by Omnic 9 (Thermo-Nicolet Instruments Co., USA) including baseline correction and Savitzky–Golay smoothing filter (set to the number of 11 points used in the algorithm).

HRMS spectrometry. HRMS spectra were recorded on a MicrOtof III (Bruker Daltonik, Bremen, Germany) with ESI or APCI ionisation sources (in positive or negative mode). For calibration of accurate masses, ESI-APCI Low Concentration Tuning Mix (Agilent) was used. The samples were delivered into the ion source in methanol or acetonitrile solution.

Synthetic procedures

Synthetic procedures for fresh 1,2,4,5-tetraaminobenzene tetrahydrochloride 3

N^1,N^3-Di-tert-butyl-4,6-dinitrobenzene-1,3-diamine 2. DFDNB **1** (1.0 g, 4.9 mmol) was dissolved in acetone (20 mL), and *tert*-butyl amine (5.4 equiv., 2.8 mL, 26.6 mmol) was added dropwise to the stirred solution. The reaction mixture was heated to reflux and stirred for 3 h. After cooling to room temperature, the solvent was removed under reduced pressure, and the resulting crude mixture was washed with cold EtOH. Compound **2** was obtained as a yellow powder (1.34 g, 88% yield). ^{1}H NMR (400 MHz, $CDCl_3$) δ: 9.28 (s, 1H, Ar*H*); 8.66 (brs, 2H, N*H*); 6.12 (s, 1H, Ar*H*); 1.53 (s, 18H, CH_3) ppm. Spectrum is in accordance with the literature.[39]

1,2,4,5-Tetraamine-benzene tetrahydrochloride 3. Compound **2** (1.13 g, 3.6 mmol) was dispersed in fuming HCl (20 mL), and $SnCl_2{\cdot}2H_2O$ (5.08 g, 22.5 mmol) was added to the stirred mixture. The reaction was heated to reflux until the formation of a white precipitate was observed. The mixture was then cooled to room temperature, and the precipitate was collected by filtration and washed with cold mixture of EtOH : ACN (9 : 1 (v : v)). Compound **3** was obtained as a white solid (0.85 g, 82%) and was used immediately in the next step due to its instability.

Synthetic procedures for tetranitro-tetraamino azacalix[4]arene skeleton 5

Acyclic precursor 4. Compound **3** (0.200 g, 0.70 mmol) was dissolved in dry acetonitrile (50 mL), and DFDNB **1** (0.287 g, 1.41 mmol) was added to the stirred solution. Before base addition, the oxygen was removed from the solution by a stream of argon. *N*,*N*-Diisopropylethylamine (1 mL, 5.7 mmol) was then added dropwise under stirring. The reaction mixture was stirred overnight at room temperature under an inert atmosphere. The next day, the solvent was removed under reduced pressure, and the crude residue was repeatedly washed with cold EtOH (100 mL). Compound **4** was obtained as a reddish powder (0.655 g, 92% yield). ^{1}H NMR (400 MHz, DMSO-d_6) δ: 9.65 (s, 2H, N*H*); 8.90 (d, 2H, Ar*H*, J = 7.9 Hz); 6.80 (s, 1H, Ar*H*); 6.53 (d, 2H, Ar*H*, J = 14.5 Hz); 6.21 (s, 1H, Ar*H*); 5.28 (s, 4H, NH_2) ppm. Spectrum is in accordance with the literature.[27]

Tetranitro-tetraamino azacalix[4]arene 5. One-pot synthesis: The procedure was described in the literature.[40]

Stepwise synthesis: The synthesis was initiated by dissolving the acyclic precursor **4** (0.125 g, 0.25 mmol) and compound **3** (0.066 g, 0.23 mmol) in dry acetonitrile (100 mL). Then, the oxygen was removed from the solution by a stream of argon, after which *N*,*N*-diisopropylethylamine (185 µL, 1.06 mmol) was added dropwise under stirring. The reaction mixture was stirred at ambient temperature for 3 h and subsequently heated to reflux overnight. After completion of the reaction, the solvent was removed under reduced pressure, and the resulting solid residue was repeatedly washed with cold EtOH (100 mL). Compound **5** was obtained as a brown powder (0.13 g, 87% yield). ^{1}H NMR (400 MHz, DMSO-d_6) δ: 8.99 (s, 2H, Ar*H*); 8.88 (s, 4H, N*H*); 6.52 (s, 2H, Ar*H*); 6.06 (s, 2H, Ar*H*); 5.69 (s, 2H, Ar*H*); 5.00 (brs, 8H, NH_2) ppm.

General procedure for ureido-based derivatives 6. Tetraamino-tetranitroazacalixarene **5** was dissolved in a mixture of DCM : EA (3 : 1 (v : v), total volume 2 mL) or in dry DMF (0.5 mL). To the stirred solution, the appropriate isocyanate (2 equiv. per free NH_2 group) was added dropwise. The reaction mixture was stirred at ambient temperature for 3 days. To quench any remaining isocyanate, MeOH (5 mL) was added, and the mixture was stirred for an additional 20 min. After completion, the solvent was removed under reduced pressure, and the resulting solid residue was purified by preparative thin-layer chromatography on silica gel, with the eluent selected according to the properties of the by-products.

*Tetra-ureido derivative **6A**.* Tetraureido derivative **6A** was prepared according to the general procedure from macrocyclic precursor **5** (56 mg, 0.09 mmol), and 4-methoxyphenyl isocyanate (95 µl, 0.74 mmol) in DMF. The residue was purified by prep-TLC (eluent DCM : MeOH; 20 : 1 (v : v)). The product **6A** was obtained as an ochreous powder (82 mg, 73%), m. p. >300 °C. ^{1}H NMR (400 MHz, DMSO-d_6) δ: 9.53 (s, 4H, N*H*); 9.10 (s, 2H, Ar*H*); 8.75 (s, 4H, N*H*); 8.69 (s, 2H, Ar*H*); 8.13 (s, 4H, N*H*); 7.27 (d, 8H, Ar*H*, J = 8.7 Hz); 7.02 (s, 2H, Ar*H*); 6.77 (d, 8H, Ar*H*; J = 9.2 Hz); 5.41 (s, 2H, Ar*H*); 3.67 (s, 12H, –OCH_3) ppm. $^{13}C\{^1H\}$ NMR (100 MHz, DMSO-d_6) δ: 154.6; 152.4; 148.5; 136.6; 132.2; 128.6; 128.1; 124.9; 122.1; 120.3; 113.9; 95.3; 55.1 ppm. IR (ATR) 3323; 3205; 3090; 3044; 3004; 2952; 2935; 2908; 2835; 1693; 1623; 1567; 1506 cm^{-1}. HRMS ESI$^+$: $(C_{56}H_{48}N_{16}O_{16} + H)^+$ m/z calcd $[M + H]^+$ 1201.3507; found 1201.3511; $(C_{56}H_{48}N_{16}O_{16} + NH_4)^+$ m/z calcd $[M + NH_4]^+$ 1218.3773; found 1218.3771.

*Tetra-ureido derivative **6B**.* Tetraureido derivative **6B** was prepared according to the general procedure from macrocyclic precursor **5** (48 mg, 0.08 mmol), and *tert*-butylphenylisocyanate (120 µl, 0.68 mmol) in mixture (DCM : EA). The residue was purified by prep-TLC (eluent DCM : MeOH; 10 : 1 (v : v)).

The product **6B** was obtained as an orange-brown powder (72.6 mg, 70%). ^{1}H NMR (400 MHz, DMSO-d_6) δ: 9.53 (s, 4H, N*H*); 9.09 (s, 2H, Ar*H*); 8.87 (s, 4H, N*H*); 8.67 (s, 2H, Ar*H*); 8.18 (s, 4H, N*H*); 7.30 (d, 8H, Ar*H*, J = 8.7 Hz); 7.20 (d, 8H, Ar*H*, J = 8.8 Hz); 7.02 (s, 2H, Ar*H*); 5.42 (s, 2H, Ar*H*); 1.21 (s, 36H, CH_3) ppm. Spectrum is in accordance with the literature.[27]

*Tetra-ureido derivative **6C**.* Tetraureido derivative **6C** was prepared according to the general procedure above from macrocyclic precursor **5** (50 mg, 0.08 mmol), and 1-naphthyl isocyanate (100 µl, 0.70 mmol) in DMF. The residue was purified by prep-TLC (eluent DCM : MeOH 40 : 1 (v : v)) or OSN (as described above). The product **6C** was obtained as a brown powder in a yield depending on the purification procedure used: 38% (prep-TLC; silica) *vs.* 82% (OSN), m. p. 282–285 °C. ^{1}H NMR (400 MHz, DMSO-d_6) δ: 9.66 (s, 4H, N*H*); 9.13 (s, 2H, Ar*H*); 9.06 (s, 4H, N*H*); 8.79 (s, 2H, Ar*H*); 8.63 (s, 4H, N*H*), 8.02–7.80 (m, 16H, Ar*H*); 7.62–7.30 (m, 12H, Ar*H*); 7.13 (s, 2H, Ar*H*), 5.56 (s, 2H, Ar*H*) ppm. ^{13}C{^{1}H} NMR (100 MHz, DMSO-d_6) δ: 153.2; 148.5; 139.1; 136.3; 128.3; 126.4; 125.9; 125.8; 125.7; 125.5; 125.2; 124.1; 123.3; 122.1; 120.0; 118.6; 118.5; 113.7; 95.3 ppm. IR (ATR) 3316; 3093; 3054; 3016; 2955; 2925; 2853; 1681; 1627; 1567; 1527; 1504 cm^{-1}. HRMS ESI$^+$: $(C_{68}H_{48}N_{16}O_{12} + H)^+$ m/z calcd $[M + H]^+$ 1281.3710; found 1281.3690; $(C_{68}H_{48}N_{16}O_{12} + Na)^+$ m/z calcd $[M + Na]^+$ 1303.3530; found 1303.3504.

*Tetra-ureido derivative **6D**.* Tetraureido derivative **6D** was prepared according to the general procedure from macrocyclic precursor **5** (52 mg, 0.09 mmol), and phenylisocyanate (75 µl, 0.69 mmol) in mixture (DCM : EA). The residue was purified by prep-TLC (eluent EA : PE; 1 : 1 (v : v)). The product **6D** was obtained as a brownish powder (71 mg, 74%), m. p. ~300 °C. ^{1}H NMR (400 MHz, DMSO-d_6) δ: 9.54 (s, 4H, N*H*); 9.10 (s, 2H, Ar*H*); 9.04 (s, 4H, N*H*); 8.71 (s, 2H, Ar*H*) 8.29 (s, 4H, N*H*); 7.38 (d, 8H, Ar*H*, J = 7.7 Hz); 7.21 (m, 8H, Ar*H*); 7.07 (s, 2H, Ar*H*); 6.92 (t, 4H, Ar*H*, J = 7.3 Hz); 5.46 (s, 2H, Ar*H*) ppm. ^{13}C{^{1}H} NMR (100 MHz, DMSO-d_6) δ: 152.3; 148.5; 139.3; 136.4; 128.7; 128.1; 125.0; 122.5; 122.0; 118.4; 118.2; 113.7; 95.3 ppm. IR (ATR) 3315; 3200; 3134; 3089; 3038; 2985; 2930; 1698; 1625; 1598; 1567; 1531 cm^{-1}. HRMS ESI$^+$: $(C_{52}H_{40}N_{16}O_{12} + Na)^+$ m/z calcd $[M + Na]^+$ 1103.2903; found 1103.2896.

*Tetra-ureido derivative **6E**.* Tetraureido derivative **6E** was prepared according to the general procedure above from macrocyclic precursor **5** (51 mg, 0.08 mmol), and 4-(trifluoromethyl) phenyl isocyanate (95 µl, 0.67 mmol) in mixture (DCM : EA). The residue was purified by prep-TLC (eluent DCM : MeOH; 40 : 1 (v : v)). The product **6E** was obtained as a dark reddish-brown powder (20 mg, 18%), m. p. >300 °C. NMR – due to strong self-aggregation ability and splitting caused by –CF_3, the ^{1}H, ^{13}C and ^{19}F spectra were not clearly resolved Fig. S18–S20. ^{1}H (400 MHz, DMSO-d_6) δ: 9.49 (s, 4H, N*H*); 9.42 (s, 4H, N*H*); 9.09 (s, 2H, Ar*H*); 8.97 (s, 2H, Ar*H*); 8.20 (s, 4H, N*H*); 7.62–7.16 (m, Ar*H*, 16H); 6.93 (s, 2H, Ar*H*); 5.20 (s, 2H, Ar*H*) ppm. ^{19}F NMR (376 MHz, DMSO-d_6) δ: −60.33 ppm. IR (ATR) 3294; 3206; 3117; 3059; 3012; 2928; 2854; 1707; 1605; 1567; 1512 cm^{-1}. HRMS ESI$^+$: $(C_{56}H_{36}F_{12}N_{16}O_{12}Na)^+$ m/z calcd $[M + Na]^+$ 1375.2399; found 1375.2402.

Supramolecular properties

Monitoring of host-host interactions

Dilution studies. The self-aggregation behavior of all prepared urea-based receptors **6** was investigated by ^{1}H NMR dilution experiments in DMSO-d_6 over a concentration range of 0.5–25.5 mM. Changes in the spectra, particularly the ureido N*H* signals, were monitored, exhibiting significant upfield shifts with decreasing concentration, indicative of aggregate dissociation. The resulting data (see pages S16–S19) were fitted using both the cooperative equal K(COEK) and dimerization/equal K(EK) models *via* the freely available Bindfit program.[30,41]

Diffusion measurements (DOSY). All experiments were performed at 298 K on a Bruker Avance DRX 500 NMR spectrometer (Karlsruhe, Germany) operating at 500.13 MHz for the ^{1}H Larmor frequency with a double-resonance broadband fluorine observe (BBFO) probe head equipped with a z-magnetic-field gradient coil (maximum gradient strength of G_{max} = 55 g cm^{-1}). ^{1}H diffusion-ordered NMR spectroscopy experiments (DOSY) were recorded using a double-stimulated echo pulse sequence incorporating bipolar gradients.[42] The acquisition of 2D DOSY spectra was performed on 20 ppm spectral width (SW), using a realaxation delay (D_1) of 3 s, 16 points in the indirect direction (F_1), 40 K complex points in the direct direction (F_2) and 32 scans (ns). Data was processed using Dynamics (T_1/T_2) module included in TopSpin 4.5.0 software ©Bruker BioSpin GmbH & Co.

Monitoring of host–guest interactions

Binding efficiency expressed by % CIS. The measurements were performed in DMSO-d_6 at a constant concentration of receptor (1.2 mM). Predefined aliquots of the anions, supplied as their tetrabutylammonium (TBA) salts, were gradually added. Based on preliminary experiments, the total amount of anion required to reach full complexation (final *CIS* value) was determined. Titration experiments were then carried out to cover the full complexation range, not just the region displayed in the main figures, ensuring saturation of binding sites. Calculation of the percentage of complexed receptor (% *CIS*) at each titration point was based on the determined minimal and maximal chemical shifts of the monitored signals (corresponding to the initial and final points of the titration equilibria). Several examples of these calculations are provided in the SI.

^{1}H NMR titrations for evaluation of apparent association constants. The numerical values of apparent association constants K_{As}(1 : 1) and overall association constants β with their errors were evaluated using the freeware program Bindfit[30] for 1 : 2 stoichiometry (receptor **6**: anion) using a statistical model. All raw data and calculation details for the individual binding events are provided in the SI.

UV-Vis measurements. UV-Vis titrations were performed in DMSO (HPLC grade 99.9%, Merck), using double beam UV-1800 spectrophotometer (Shimadzu). Titrations were standardly performed at a constant concentration of receptor **6** (reported for specific measurements in SI; Fig. S31–S37).

Spectra were recorded over the wavelength range 270–800 nm with 1 nm increments, using quartz cuvettes with a 1-mm path length.

Computational details

All molecular dynamics simulations were performed at the all-atom level using the AMBER 2025 software package.[43] The initial dimer geometries of **6B** and **6C** were energy-minimized and then solvated in cubic boxes of explicit DMSO molecules, ensuring a minimum distance of 12 Å between the solute and the box boundary.

Bonded and nonbonded parameters for the receptors were assigned using the general AMBER force field for organic molecules (GAFF),[44] following the standard AmberTools 2025[43] parametrization workflow. Partial atomic charges were assigned using the AM1-BCC scheme as implemented in the *antechamber module* of AmberTools 2025, and any missing parameters were generated within the GAFF framework. All simulations were conducted under periodic boundary conditions.

After energy minimization, the systems were equilibrated in two stages: (i) NVT equilibration at 298 K using a Langevin thermostat[45] (collision frequency 2.5 ps^{-1}), followed by (ii) NPT equilibration at 1 atm using a Berendsen barostat[46] to adjust the box volume. Production MD simulations were carried out for 500 ns for each system. No predefined production window was excluded from analysis, as the objective was to monitor the full-time evolution of dimer stability. All structural descriptors and energetic analyses were therefore performed over the entire 500 ns trajectories. A time step of 2 fs was used, and all covalent bonds involving hydrogens were constrained *via* the SHAKE algorithm.[47] Long-range electrostatics were treated with the particle mesh Ewald method,[48] with a real-space cutoff of 10 Å.

Appropriate counterions were added when required to maintain electroneutrality.

Analysis of the trajectories focused on structural descriptors relevant to supramolecular association. The total number of intradimer hydrogen-bond (HB) contacts was computed using standard geometric criteria (donor–acceptor distance ≤3.5 Å and H–D–A angle ≥135°), without predefining specific donor–acceptor pairs. The native-contact fraction (Q) was calculated by monitoring intermonomer heavy-atom contacts within a cutoff distance of 4.5 Å, relative to the initial dimer structure. The center-of-mass distance ($d_{COM-COM}$) between the macrocycles was evaluated along the trajectories to quantify association stability. π–π stacking parameters (interplanar distance and angle between the aromatic platforms) were obtained by least-squares plane fitting.

To estimate the thermodynamic stability of the dimers, an MM/PBSA approach[32] was applied using a single-trajectory protocol. Snapshots were extracted every 10 ps from the full 500 ns trajectories, resulting in 50 000 frames for each system. The binding enthalpy (ΔH) was computed as the sum of van der Waals (ΔE_{vdW}), electrostatic (ΔE_{ele}), internal (ΔE_{int}), polar solvation (ΔGPB), and nonpolar solvation (ΔG_{NP}) contributions. Entropic contributions ($T\Delta S$) were evaluated by quasi-harmonic analysis[49] of the covariance matrix of atomic fluctuations. The free energy of binding was then computed as $\Delta G = \Delta H - T\Delta S$. Reported uncertainties correspond to standard deviations over the sampled frames.

All trajectory and structural analyses were performed with AmberTools 2025 and in-house Python scripts on the Leonardo supercomputer (CINECA, Bologna, Italy) and on in-house CPU/GPU hybrid cluster. Graphs were produced using GraphPad Prism (version 10 for macOS, GraphPad Software, Boston, Massachusetts USA, **https://www.graphpad.com**). Visual inspection and rendering of representative structures were carried out with UCSF Chimera.[50]

X-Ray diffraction

The crystal of sufficient quality was selected in sample **6C** placed on glass fibre and measured at 100 (2) K on a Rigaku OD Synergy diffractometer, with micro-focused rotating anode X-ray tube (Cu-Kα λ = 1.54184 Å) and highly sensitive HyPix-Arc 150° photon counting detector. The data collection, absorption correction and scaling were handled in CrysAlisPRO.[51] M = 1646.71 g mol^{-1}, monoclinic system, space group $P2_1/n$, a = 19.2709 (4) Å, b = 23.7185 (3) Å, c = 19.4770 (3) Å, β = 118.701 (2)°, Z = 4, V = 7808.7 (3) $Å^3$, D_c = 1.401 g cm^{-3}, μ(Cu-Kα) = 0.84 mm^{-1}, crystal dimensions 0.16 × 0.04 × 0.03 mm. The structure was solved by charge flipping methods[52] and anisotropically refined by full matrix least squares on F squared using the Crystals[53] to final value R = 0.054 and wR = 0.165 using 15 517 independent reflections (θ_{max} = 73.5°), 1310 parameters and 528 restrains. The hydrogen atoms were placed in calculated positions refined with riding constraints. One naphthyl group and one ureido group were found to be disordered over two positions. In both cases the atomic positions of second positions were found in difference electron density maps and refined with restrained geometry and ADPs. In both cases the occupancies were refined with sum constrained to 1, resulting in occupancy ratios of 537(4) : 463(4) for naphthyl and 918(3) : 82(3) for ureido group. The residual electron density maps were visualized in MCE.[54] The molecular graphics were created using Diamond 3.0.[55] The structure was deposited into Cambridge Structural Database under number CCDC 2538630. For numbering schemes and disorder descriptions see SI.

Author contributions

Karolína Salvadori: synthesis, data curation, investigation of host-host and host–guest behaviour, conceptualization, writing – original draft, funding acquisition. Sabrina Pricl: MD calculation, writing – original draft. Aura Tintaru: DOSY measurements. Alena Krupková: nanofiltation, writing – review & editing. Václav Eigner: X-ray analysis. Pavel Matějka: writing – review & editing. Pavel Lhoták: graphics, writing – review & editing. Olivier Siri: writing – review & editing, supervision, funding acquisition.

Conflicts of interest

There are no conflicts of interest to declare.

Data availability

The data supporting this article have been included as part of the supplementary information (SI). Supplementary information: spectral characterization of new compounds, dilution experiments, complexation data, MD simulations, and X-ray data. See DOI: **https://doi.org/10.1039/d6qo00354k**.

CCDC 2538630 contains the supplementary crystallographic data for this paper.[56]

Acknowledgements

K. S. acknowledges financial support provided by Czech Science Foundation (Grant 25-17173O); O. S. sincerely thanks the CNRS and the French Ministry of Research and Higher Education for their support. The crystallographic part of this work was supported by the project TERAFIT CZ.02.01.01/00/22_008/0004594 (V. E.).

References

1 E. Takeda, Y. Taketani, N. Sawada, T. Sato and H. Yamamoto, The regulation and function of phosphate in the human body, *BioFactors*, 2004, **21**, 345–355, DOI: **10.1002/biof.552210167**.

2 M. R. Hart, B. F. Quin and M. L. Nguyen, Phosphorus runoff from agricultural land and direct fertilizer effects: a review, *J. Environ. Qual.*, 2004, **33**, 1954–1972, DOI: **10.2134/jeq2004.1954**.

3 I. A. Veselova, E. A. Sergeeva, M. I. Makedonskaya, O. E. Eremina, S. N. Kalmykov and T. N. Shekhovtsova, Methods for determining neurotransmitter metabolism markers for clinical diagnostics, *J. Anal. Chem.*, 2016, **71**, 1155–1168, DOI: **10.1134/S1061934816120108**.

4 S. Net, A. Delmont, R. Sempéré, A. Paluselli and B. Ouddane, Reliable quantification of phthalates in environmental matrices (air, water, sludge, sediment and soil): a review, *Sci. Total Environ.*, 2015, **515–516**, 162–180, DOI: **10.1016/j.scitotenv.2015.02.013**.

5 (*a*) P. Molina, F. Zapata and A. Caballero, Anion recognition strategies based on combined noncovalent interactions, *Chem. Rev.*, 2017, **117**, 9907–9972, DOI: **10.1021/acs.chemrev.6b00814**; (*b*) D. A. McNaughton, W. G. Ryder, A. M. Gilchrist, P. Wang, M. Fares, X. Wu and P. A. Gale, New insights and discoveries in anion receptor chemistry, *Chem*, 2023, **9**, 3045–3112, DOI: **10.1016/j.chempr.2023.07.006**.

6 S. C. Patrick, P. D. Beer and J. J. Davis, Solvent effects in anion recognition, *Nat. Rev. Chem.*, 2024, **8**, 256–276, DOI: **10.1038/s41570-024-00584-4**.

7 B. P. Hay, T. K. Firman and B. A. Moyer, Structural design criteria for anion hosts: strategies for achieving anion shape recognition through the complementary placement of urea donor groups, *J. Am. Chem. Soc.*, 2005, **127**, 1810–1819, DOI: **10.1021/ja043995k**.

8 D. Barišić, F. Lešić, M. T. Vlašić, K. Užarević, N. Bregović and V. Tomišić, Anion binding by receptors containing NH donating groups – what do anions prefer?, *Tetrahedron*, 2022, **120**, 132875, DOI: **10.1016/j.tet.2022.132875**.

9 D. E. Gómez, L. Fabbrizzi, M. Licchelli and E. Monzani, Urea vs. thiourea in anion recognition, *Org. Biomol. Chem.*, 2005, **3**, 1495–1500, DOI: **10.1039/B500123D**.

10 C. Caltagirone, G. W. Bates, P. A. Gale and M. E. Light, Anion binding vs. sulfonamide deprotonation in functionalised ureas, *Chem. Commun.*, 2008, 61–63, DOI: **10.1039/B713431B**.

11 R. Moral, O. A. Pegu and G. Das, Terminal substituent-induced differential aggregation and sensing properties: a case study of neutral benzimidazole-based urea receptors, *New J. Chem.*, 2023, **47**, 19625–19632, DOI: **10.1039/D3NJ03806H**.

12 M. Takahashi, N. Ito, N. Haruta, H. Ninagawa, K. Yazaki, Y. Sei, T. Sato and M. Obata, Environment-sensitive emission of anionic hydrogen-bonded urea-derivative–acetate-ion complexes and their aggregation-induced emission enhancement, *Commun. Chem.*, 2021, **4**, 168, DOI: **10.1038/s42004-021-00601-3**.

13 M. Boiocchi, L. Del Boca, D. E. Gómez, L. Fabbrizzi, M. Licchelli and E. Monzani, Nature of urea-fluoride interaction: incipient and definitive proton transfer, *J. Am. Chem. Soc.*, 2004, **126**, 16507–16514, DOI: **10.1021/ja045936c**.

14 U. Manna, B. Portis, T. K. Egboluche, M. Nafis and M. A. Hossain, Anion binding studies of urea and thiourea functionalized molecular clefts, *Front. Chem.*, 2021, **8**, 575701, DOI: **10.3389/fchem.2020.575701**.

15 C. Jia, B. Wu, S. Li, X. Huang, Q. Zhao, Q.-S. Li and X.-J. Yang, Highly efficient extraction of sulfate ions with a tripodal hexaurea receptor, *Angew. Chem., Int. Ed.*, 2011, **50**, 486–490, DOI: **10.1002/anie.201004461**.

16 S. K. Dey, B. Gil-Hernández and P. Kumar, Anion recognition-induced selective separation of phosphates from complex aqueous matrices by self-assembled molecular capsule, *Eur. J. Org. Chem.*, 2025, e202500403, DOI: **10.1002/ejoc.202500403**.

17 P. S. Lakshminarayanan, I. Ravikumar, E. Suresh and P. Ghosh, Trapped inorganic phosphate dimer, *Chem. Commun.*, 2007, 5214–5216, DOI: **10.1039/B713365K**.

18 (*a*) K. Salvadori, A. Krupková, L. Šťastná, M. Müllerová, V. Eigner, T. Strašák and P. Cuřínová, Controlled anchoring of (phenylureido)sulfonamide-based receptor moieties: an impact of binding site multiplication on complexation properties, *Molecules*, 2021, **26**, 5670, DOI: **10.3390/molecules26185670**; (*b*) K. Salvadori, A. Onali, G. Mathez, V. Eigner, M. Dendisová, P. Matějka, M. Mullerová, A. Brancale and P. Cuřínová, An insight into anion extrac-

tion by amphiphiles: hydrophobic microenvironments as a requirement for the extractant selectivity, *ACS Omega*, 2023, **8**, 44221–44228, DOI: 10.1021/acsomega.3c06767.

19 T. K. Lindhorst and C. Kieburg, Glycocoating of oligovalent amines: synthesis of thiourea-bridged cluster glycosides from glycosyl isothiocyanates, *Angew. Chem., Int. Ed. Engl.*, 1996, **35**, 1953–1956, DOI: 10.1002/anie.199619531.

20 M. J. Mayoral, N. Bilbao and D. González-Rodríguez, Hydrogen-bonded macrocyclic supramolecular systems in solution and on surfaces, *ChemistryOpen*, 2016, **5**, 10–32, DOI: 10.1002/open.201500171.

21 J. Svec, M. Necas and V. Sindelar, Bambus[6]uril, *Angew. Chem., Int. Ed.*, 2010, **49**, 2378–2381, DOI: 10.1002/anie.201000420.

22 A. Zhang, Y. Han, K. Yamato, X. C. Zeng and B. Gong, Aromatic oligoureas: enforced folding and assisted cyclization, *Org. Lett.*, 2006, **8**, 803–806, DOI: 10.1021/ol0526322.

23 S. Dawn, M. B. Dewal, D. Sobransingh, M. C. Paderes, A. C. Wibowo, M. D. Smith, J. A. Krause, P. J. Pellechia and L. S. Shimizu, Self-assembled phenylethynylene bis-urea macrocycles facilitate the selective photodimerization of coumarin, *J. Am. Chem. Soc.*, 2011, **133**, 7025–7032, DOI: 10.1021/ja110779h.

24 J. Budka, P. Lhoták, V. Michlová and I. Stibor, Urea derivatives of calix[4]arene 1,3-alternate: an anion receptor with profound negative allosteric effect, *Tetrahedron Lett.*, 2001, **42**, 1583–1586, DOI: 10.1016/S0040-4039(00)02309-1.

25 K. D. Shimizu and J. Rebek, Synthesis and assembly of self-complementary calix[4]arenes, *Proc. Natl. Acad. Sci. U. S. A.*, 1995, **92**, 12403–12407, DOI: 10.1073/pnas.92.26.12403.

26 M. Yokoya, S. Kimura and M. Yamanaka, Urea derivatives as functional molecules: supramolecular capsules, supramolecular polymers, supramolecular gels, artificial hosts, and catalysts, *Chem. – Eur. J.*, 2021, **27**, 5601–5614, DOI: 10.1002/chem.202004367.

27 K. Salvadori, P. Matějka, P. Lhoták and O. Siri, Amplified recognition of basic anions induced by cooperative interaction of ureido-binding sites preorganized by azacalix[4]arene skeleton, *J. Org. Chem.*, 2026, **91**, 1503–1512, DOI: 10.1021/acs.joc.5c02079.

28 H. Konishi, S. Hashimoto, T. Sakakibara, S. Matsubara, Y. Yasukawa, O. Morikawa and K. Kobayashi, Synthesis and conformational properties of tetranitroazacalix[4]arenes, *Tetrahedron Lett.*, 2009, **50**, 620–623, DOI: 10.1016/j.tetlet.2008.11.095.

29 A. Krupková, M. Müllerová, R. Petrickovic and T. Strašák, On the edge between organic solvent nanofiltration and ultrafiltration: characterization of regenerated cellulose membrane with aspect on dendrimer purification and recycling, *Sep. Purif. Technol.*, 2023, **310**, 123141, DOI: 10.1016/j.seppur.2023.123141.

30 P. Thordarson, *BindFit: a web-based tool for the analysis of binding data*, https://supramolecular.org, accessed March 2026.

31 L. Avram and Y. Cohen, Diffusion NMR of molecular cages and capsules, *Chem. Soc. Rev.*, 2015, **44**, 586–602, DOI: 10.1039/C4CS00197D.

32 P. A. Kollman, I. Massova, C. Reyes, B. Kuhn, S. Huo, L. Chong, M. Lee, T. Lee, Y. Duan, W. Wang, O. Donini, P. Cieplak, J. Srinivasan, D. A. Case and T. E. Cheatham, Calculating structures and free energies of complex molecules: combining molecular mechanics and continuum models, *Acc. Chem. Res.*, 2000, **33**, 889–897, DOI: 10.1021/ar000033j.

33 J. M. Živković, I. M. Stanković, D. B. Ninković and S. D. Zarić, Decisive influence of environment on aromatic/aromatic interaction geometries. Comparison of aromatic/aromatic interactions in crystal structures of small molecules and in protein structures, *Cryst. Growth Des.*, 2021, **21**, 1898–1904, DOI: 10.1021/acs.cgd.0c01514.

34 M. O. Sinnokrot and C. D. Sherrill, Substituent effects in π–π interactions: sandwich and T-shaped configurations, *J. Am. Chem. Soc.*, 2004, **126**, 7690–7697, DOI: 10.1021/ja049434a.

35 K. Hirose, in *Analytical Methods in Supramolecular Chemistry*, 2012, DOI: 10.1002/9783527644131.ch2.

36 P. Job, *Ann. Chim.*, 1928, **10**, 113–203.

37 C. Wang, M. Du, F. Ruan, Y. He, Y. Cai, L. Kong and X. Hu, Exploiting the dimerization characteristic of $H_2PO_4^-$ to promote its selective recognition by a tetra-amido macrocycle, *J. Org. Chem.*, 2025, **90**, 6468–6477, DOI: 10.1021/acs.joc.5c00279.

38 L. K. S. von Krbek, C. A. Schalley and P. Thordarson, Assessing cooperativity in supramolecular systems, *Chem. Soc. Rev.*, 2017, **46**, 2622–2637, DOI: 10.1039/C7CS00063D.

39 T. Munteanu, V. Mazan, M. Elhabiri, C. Benbouziyane, G. Canard, D. Jacquemin, O. Siri and S. Pascal, A strategy to design substituted tetraamino-phenazine dyes and access to an NIR-absorbing benzoquinonediimine-fused quinoxaline, *Org. Lett.*, 2023, **25**, 3886–3891, DOI: 10.1021/acs.orglett.3c01251.

40 Z. Chen, M. Giorgi, D. Jacquemin, M. Elhabiri and O. Siri, Azacalixphyrin: the hidden porphyrin cousin brought to light, *Angew. Chem., Int. Ed.*, 2013, **52**, 6250–6254, DOI: 10.1002/anie.201301217.

41 K. W. K. Tong, S. Dehn, J. E. A. Webb, K. Nakamura, F. Braet and P. Thordarson, Pyromellitamide gelators: exponential rate of aggregation, hierarchical assembly, and their viscoelastic response to anions, *Langmuir*, 2009, **25**, 8586–8592, DOI: 10.1021/la804180h.

42 D. H. Wu, A. D. Chen and C. S. Johnson, An improved diffusion-ordered spectroscopy experiment incorporating bipolar-gradient pulses, *J. Magn. Reson., Ser. A*, 1995, **115**, 260–264, DOI: 10.1006/jmra.1995.1176.

43 D. A. Case, H. M. Belfon, K. Ben-Shalom, I. Y. Berryman and J. T. Brozell, *et al.*, *AMBER 2025*, University of California, San Francisco, 2025.

44 J. Wang, R. M. Wolf, J. W. Caldwell, P. A. Kollman and D. A. Case, Development and testing of a general AMBER force field, *J. Comput. Chem.*, 2004, **25**, 1157–1174, DOI: 10.1002/jcc.20035.

45 R. J. Loncharich, B. R. Brooks and R. W. Pastor, Langevin dynamics of peptides: the frictional dependence of isomer-

ization rates of N-acetylalanyl-N′-methylamide, *Biopolymers*, 1992, **32**, 523–535, DOI: **10.1002/bip.360320508**.

46 H. J. C. Berendsen, J. P. M. Postma, W. F. van Gunsteren, A. DiNola and J. R. Haak, Molecular dynamics with coupling to an external bath, *J. Chem. Phys.*, 1984, **81**, 3684–3690, DOI: **10.1063/1.448118**.

47 J.-P. Ryckaert, G. Ciccotti and H. J. C. Berendsen, Numerical integration of the cartesian equations of motion of a system with constraints: molecular dynamics of n-alkanes, *J. Comput. Phys.*, 1977, **23**, 327–341, DOI: **10.1016/0021-9991(77)90098-5**.

48 T. Darden, D. York and L. Pedersen, Particle mesh Ewald: an N·log(N) method for Ewald sums in large systems, *J. Chem. Phys.*, 1993, **98**, 10089–10092, DOI: **10.1063/1.464397**.

49 I. Andricioaei and M. Karplus, On the calculation of entropy from covariance matrices of the atomic fluctuations, *J. Chem. Phys.*, 2001, **115**, 6289–6292, DOI: **10.1063/1.1401821**.

50 E. F. Pettersen, T. D. Goddard, C. C. Huang, G. S. Couch, D. M. Greenblatt, E. C. Meng and T. E. Ferrin, UCSF Chimera—a visualization system for exploratory research and analysis, *J. Comput. Chem.*, 2004, **25**, 1605–1612, DOI: **10.1002/jcc.20084**.

51 Rigaku OD, *CrysAlisPro*, Rigaku Oxford Diffraction Ltd, Yarnton, Oxfordshire, England, 2020.

52 L. Palatinus and G. Chapuis, *J. Appl. Crystallogr.*, 2007, **40**, 786–790, DOI: **10.1107/S0021889807029238**.

53 P. W. Betteridge, J. R. Carruthers, R. I. Cooper, K. Prout and D. J. Watkin, *J. Appl. Crystallogr.*, 2003, **36**, 1487, DOI: **10.1107/S0021889803021800**.

54 J. Rohlíček and M. Hušák, *J. Appl. Crystallogr.*, 2007, **40**, 600–601, DOI: **10.1107/S0021889807018894**.

55 K. Brandenburg, *DIAMOND*, Crystal Impact GbR, Bonn, Germany, 1999.

56 CCDC 2538630: Experimental Crystal Structure Determination, 2026, DOI: **10.5517/ccdc.csd.cc2r6n9y**.